



High-sensitivity U–Pb rutile dating by secondary ion mass spectrometry (SIMS) with an O_2^+ primary beam

Axel K. Schmitt ^{a,*}, Thomas Zack ^{b,1}

^a Department of Earth and Space Sciences, University of California Los Angeles, 595 Charles Young Dr. E, Geology Building 3806, Los Angeles, CA 90095, USA

^b Institut für Geowissenschaften, Universität Mainz, Becher Weg 21, 55128 Mainz, Germany

ARTICLE INFO

Article history:

Received 21 July 2012

Received in revised form 1 September 2012

Accepted 1 September 2012

Available online 19 September 2012

Editor: K. Mezger

Keywords:

Rutile

Geochronology

U–Pb

Ion microprobe

Orientation effects

ABSTRACT

We present a secondary ionization mass spectrometry (SIMS) technique for U–Pb geochronology of rutile at high spatial resolution and sensitivity using an O_2^+ primary ion beam coupled with surficial O_2 gas deposition (O_2 flooding). The O_2^+ beam is $\sim 10\times$ more intense than conventionally applied O^- or O_2^- beams at the same lateral resolution. Natural and synthetic rutile was determined to be conductive under O_2^+ bombardment, permitting higher excavation (sputter) rates than conventional SIMS using negatively charged O-beams without detrimental effects of sample charging. The main advantage of O_2^+ is rapid sputtering at shallow primary ion penetration depths. This minimizes the contribution of surface-derived common Pb, and generates a high secondary ion flux at high sensitivity with useful yields ($UY = \text{detected ions/atoms removed from target}$) for Pb in rutile of ~ 4 and 3% for O^- and O_2^+ , respectively. In addition, O_2 flooding reduces spread in the Pb^+/U^+ vs. UO_2^+/U^+ calibration by mitigating crystal orientation dependent variability of sputter yields. Calibrated against primary rutile standard R10b (1090 Ma), O_2^+ -generated SIMS U–Pb and Pb–Pb age averages are accurate within $<1\%$ for Early Paleozoic to Archean rutile, without evidence for significant crystal orientation bias. We propose that O_2^+ bombardment can also be advantageous for SIMS analysis of other conductive minerals such as cassiterite, columbite–tantalite, hematite, ilmenite, and magnetite.

© 2012 Elsevier B.V. All rights reserved.

1. Introduction

Rutile (TiO_2) commonly crystallizes as an accessory mineral under high grade metamorphic conditions where it dominates the budget of many high field strength elements (e.g., Nb, Ta, Zr, Hf, Sn, W; Foley et al., 2000; Klemme et al., 2005; Zack et al., 2002). Rutile also remains stable under near-surface conditions so that it is preserved in the detrital record (e.g., Zack et al., 2004b; Harrison et al., 2007; Meinhold, 2010). Initial U/Pb (and U/Th) is high in rutile (e.g., Klemme et al., 2005) which permits rutile to be used as a geochronometer. Pioneering studies applied thermal ionization mass spectrometry (TIMS) analysis of rutile separates to constrain metamorphic cooling histories (e.g., Mezger et al., 1989) or eruption of xenolith-bearing kimberlites (e.g., Davis, 1997). More recently, high spatial resolution U–Th–Pb dating techniques (laser ablation inductively coupled plasma mass spectrometry LA-ICP-MS) and SIMS (secondary ionization mass spectrometry) have been developed for in-situ and detrital rutile geochronology (e.g., Vry and Baker, 2006; Kooijman et al., 2010; Li et al., 2011; Zack et al., 2011; Taylor et al., 2012). Further refinement of such techniques is the key for enabling dating of small crystals or

heterogeneous rutile crystal domains and low radiogenic Pb rutile, as well as rapid analysis of individual crystals at high spatial resolution as a prerequisite for reliably characterizing detrital rutile populations.

The high spatial resolution techniques dominantly applied in isotopic dating of accessory minerals, LA-ICP-MS and SIMS, are largely complementary: LA-ICP-MS is capable of rapid sampling (via ablation), albeit at comparatively low sensitivity, whereas SIMS offers an intrinsically higher spatial resolution and sensitivity, but its throughput is restricted by relatively low signal intensities resulting from smaller rates of mass removal (via sputtering). For U–Th–Pb dating of geological materials (mostly silicates and phosphates), SIMS applications have exclusively utilized primary ion beams of negatively charged oxygen (O^- or O_2^- which in modern instrumentation are mass-filtered for dominant ^{16}O to exclude OH; henceforth, we use O as shorthand for ^{16}O). With few exceptions (e.g., Genareau et al., 2007), O_2^+ primary ion sputtering has rarely been applied to geologic materials because of difficulties in preventing localized charging in insulators (cf. Pivovarov et al., 2004). This restriction is unfortunate because the positive aspects of high O_2^+ brilliance of the duoplasmatron ion source, high sputter rates, high depth resolution, and ease of operation have been harnessed for over 30 years in SIMS depth-profiling of semiconductor materials (e.g., Hunter, 2009).

Natural rutile incorporates trace OH^- and Fe^{3+} (e.g., Bromiley and Hilairret, 2005; Colasanti et al., 2011), introducing lattice defects, which in doped synthetic rutile is known to cause semiconductivity

* Corresponding author. Tel.: +1 310 206 5760; fax: +1 310 825 2677.

E-mail addresses: axel@oro.ess.ucla.edu (A.K. Schmitt), zack@uni-mainz.de (T. Zack).

¹ Tel.: +49 6131–3920476.

(e.g., Nowotny et al., 2008). Here, we report that natural rutile from a wide variety of geological conditions behaves conductively under O_2^+ bombardment. Consequently secondary ion signals are stable during O_2^+ sputtering without any additional measures for charge compensation, similar to SIMS analysis of synthetic TiO_2 (Kitagawa et al., 2010). Through cross-calibration between rutiles of known age, we demonstrate that this technique can provide accurate Pb–Pb ages that are more precise than those of conventional SIMS analysis with an O^- beam. U–Pb ages are nearly equivalent in precision and accuracy for both primary ion beams, with the advantage of a faster sputter rate and thus higher secondary ion signal afforded by the O_2^+ beam. Fast sputtering at high secondary ion yields also extends the applicability of conventional SIMS rutile analysis into the realm of low Pb/U and rapid-throughput detrital geochronology.

2. Rutile reference materials

Compared to zircon, development of rutile reference materials is still in an early stage. However, we have access to material from three localities where rutile samples have been dated by isotope dilution (ID) TIMS (Gjerstad, Blumberg, and Windmill Hills). In the course of this study, potentially suitable material was also investigated from other localities (Giftkuppe, Musina) where ID TIMS ages are still lacking.

2.1. R10b

One single $\sim 1\text{ cm}^3$ crystal from Gjerstad (Norway) has been characterized as homogeneous in the abundances of several trace elements (e.g., $\sim 50\text{ ppm U}$) in its core, and is hence used as a trace element mineral standard (Luvizotto et al., 2009). ID TIMS U–Pb geochronology of several fragments yielded a concordant age of $1090 \pm 5\text{ Ma}$ (Luvizotto et al., 2009). For this study, a second $\sim 1\text{ cm}^3$ crystal was found to be indistinguishable in terms of trace element composition, and its U–Pb ages are identical to R10 within the limits of LA-ICP-MS precision (T. Zack, unpublished data). We therefore adopt the ID TIMS age of R10 to R10b. Further larger crystals from the same location are currently under investigation with the aim of establishing Gjerstad as a prime source for rutile reference material.

2.2. R19

Another $\sim 1\text{ cm}^3$ sized single crystal from the study of Luvizotto et al. (2009) has been characterized as a U–Pb age standard for in-situ rutile dating. It originates from Blumberg (Australia), and has been ID TIMS dated at $489.5 \pm 0.9\text{ Ma}$ (Zack et al., 2011). Because it is younger and lower in U ($\sim 15\text{ ppm}$) compared to R10, it is a good example of rutile with comparatively low radiogenic Pb. We included it here to test the suitability of SIMS dating of such low Pb/U rutiles.

2.3. JIMP-1B

Rutile crystals have been extracted from a coarse-grained quartzite sample (JIMP-1B) from the same location as the sample WHQ (Windmill Hills, Australia) that is used as the primary rutile reference material at the SHRIMP laboratory in Perth (e.g., Taylor et al., 2012). An ID-TIMS age of 2625 Ma has been cited from unpublished data by Clark et al. (2000), without stated error.

2.4. Other rutiles

In addition to the ID TIMS age-referenced rutiles, we included a variety of natural and synthetic rutiles to examine the potential for 1) variable electrical properties and 2) variable isobaric interferences resulting from changing trace element abundances. These comprise

R13 (Giftkuppe, Namibia), SQR36 (Musina locality, Limpopo Belt, South Africa), and synthetic rutile (Sy; Luvizotto et al., 2009).

3. SIMS instrumental conditions

3.1. O^- primary ion beam

Instrumental conditions for O^- primary beam bombardment of rutile using the UCLA CAMECA ims1270 (Table 1) are equivalent to those routinely applied for U–Pb zircon geochronology. The Z-electrode position of a hollow cathode duoplasmatron ion source was positioned below the central axis to avoid extraction of secondary electrons, which are also separated from O^- by a strong axis-parallel magnetic field (Coath and Long, 1995). The magnetic field was generated by an adjustable coil operated near the current maximum producing a nominal magnetic field of $\sim 740\text{ G}$ (G. Jarzebinski, pers. comm.). O^- ions were extracted at -12.5 kV , and focused to an aperture-limited (Köhler illumination) spot on the sample surface held at a potential of $+10\text{ kV}$ (total impact energy 22.5 keV). The O^- primary beam current was $\sim 19\text{ nA}$, producing a $\sim 20 \times 35\text{ }\mu\text{m}$ oval spot (Fig. 1). Positive secondary ions were transferred into the mass spectrometer via an aperture (field aperture) which was set to approximate the dimensions of the analysis crater. The secondary ion energy bandpass was 50 eV , and the mass spectrometer was tuned to a mass resolving power ($MRP = M/\Delta M$ at 10% of the peak maximum) of 4500, sufficient to resolve molecular interferences on the isotopes of interest (e.g., $^{176}\text{HfO}_2$ on ^{208}Pb ; Fig. 2D).

3.2. O_2^+ primary ion beam

For O_2^+ analysis, the polarity of the duoplasmatron and primary ion column was switched to positive (Table 1). To efficiently extract O_2^+ , the Z-electrode was centered, and the coil current reduced to $\sim 25\%$ of the O^- coil setting. The duoplasmatron extraction potential

Table 1
SIMS parameters for U–Pb rutile analysis.

	O^- beam	O_2^+ beam
<i>Duoplasmatron</i>		
Arc current (mA)	75.0	50.0
Coil (% max. current)	75	20
Extraction voltage (kV)	-12.5	$+15.5$
<i>Primary beam</i>		
Illumination	Köhler ^a	Gaussian ^b
Spot diameter (μm)	20×35	35
Average current (nA)	19	130
<i>Sample and secondary beam</i>		
Sample voltage (kV)	$+10.0$	$+4.5$
Distance from extraction plate (mm)	6.0	5.0
O_2 pressure (Torr)	5×10^{-6}	1×10^{-5}
Field of view (μm)	150	150
Contrast aperture diameter (μm)	400	400
Field aperture width (μm)	4000	3000
Energy bandpass (eV)	50	50
Mass resolution power ($M/\Delta M$)	4500	4500
<i>Sputtering and sensitivity</i>		
Average pit depth after 12 min (μm)	1.5	8.0
Volumetric sputter rate ($\mu\text{m}^3/\text{s/nA}$)	0.06 ^a	0.03 ^b
Depth sputter rate (nm/s/nA)	0.11	0.08
Sputter yield ^c	0.74	0.24
Useful yield ^d % $^{206}\text{Pb}^+$	3.6	2.7
Useful yield ^d % $^{238}\text{U}^+$	0.02	0.02
Useful yield ^d % $^{238}\text{UO}_2^+$	1.7	1.3

Averages for R10b rutile; 50 ppm U ; $^{206}\text{Pb}/^{238}\text{U} = 0.185$; $\rho = 4.23\text{ g/cm}^3$.

^a Cylindrical crater geometry.

^b Conical crater geometry.

^c Sample atoms removed per incoming oxygen.

^d Number of ions detected per atom of the same element sputtered from the sample, adjusted for 60% smaller field aperture area used for O_2^+ .

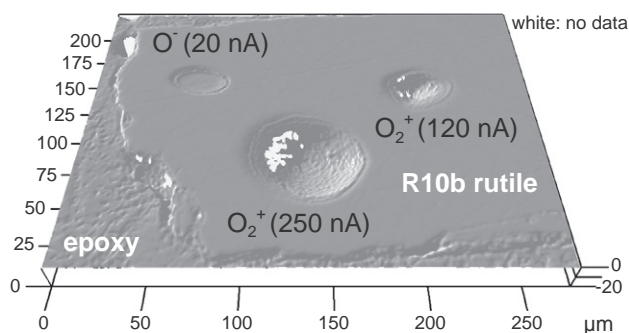


Fig. 1. MicroXAM surface topography map of rutile R10b (grain 12) embedded in epoxy. SIMS analysis craters were generated by different primary ion beams with identical sputter durations (~12 min).

for O_2^+ was +15.5 kV and the sample potential was set to +4.5 kV (total impact energy 11 keV). The resulting total O_2^+ emission current was approximately 10-times higher than for O^- (we note that the primary column Faraday cup on the ims1270 overcounts O_2^+ because of unsuppressed secondary electron emission; actual currents are ~70% of its read-out based on an intercalibration with a Faraday cup placed in the sample position). The primary ion beam was initially tuned to an aperture-limited (Köhler illumination) $\sim 30 \times 40 \mu\text{m}$ spot at $\sim 200 \text{ nA } O_2^+$, but because of rapid erosion of the aperture under intense O_2^+ bombardment, the spot increased to $\sim 45 \times 60 \mu\text{m}$ over the course of a 24 h analysis session (Fig. 1). Subsequently, the primary column was retuned to obtain a critical (Gaussian) O_2^+ beam. This beam is largely unrestricted by apertures, and a stable beam current of $\sim 120 \text{ nA}$ was obtained which resulted in an $\sim 35 \mu\text{m}$ wide (at the surface) conical crater without degradation of the spatial resolution over a 24 h period (Fig. 1). The secondary column was tuned to meet the same MRP criteria outlined above, except for narrowing the field aperture for the Gaussian beam to admit only ions emitted

from the inner $\sim 15 \mu\text{m}$ of the analysis crater, and to exclude surficial common Pb derived from the more slowly sputtered edges. The secondary ion detection protocol was identical to that used for the O^- primary beam.

3.3. Mounting procedure and acquisition conditions

A single mount was prepared that contained multiple grains of all standards characterized above. Through manipulation with a picking needle on adhesive tape, we attempted to randomly orient individual crystals based on their morphology because Taylor et al. (2012) reported orientation dependent spread along their Pb/U calibration. After casting the grains in Buehler Epoxycure epoxy, the mount was sectioned using 1200 grit SiC paper and $3 \mu\text{m}$ polyethylene-backed diamond abrasive sheets to ensure flatness of the surface. The mount was ultrasonically cleaned using detergent, 1 N HCl, deionized water, and methanol, and subsequently coated with an $\sim 20\text{--}30 \text{ nm}$ thick conductive Au layer. After an overnight pump-out at high vacuum, the mount was transferred into the ims1270 sample chamber.

All analyses followed an automated protocol of (1) primary ion beam intensity measurement (before and after the analysis), (2) surface pre-sputtering, (3) centering of the transfer deflectors, (4) magnetic field centering (using abundant Ti_3O_4 as a reference for low-intensity mass peaks; Fig. 2), (5) scanning the sample high voltage on UO_2^+ to compensate for differential charging of the analysis spots (by adjusting the secondary extraction potential to the flat part of the secondary ion energy distribution of UO_2^+ with a 7 eV energy gap at a 50 eV bandpass; a -35 V offset was applied for analysis of U^+ ; Fig. 3). After these initial routines lasting a total of $\sim 200 \text{ s}$, secondary ions were then counted with a single ETP electron multiplier by cycling the magnetic field 10 times and integrating counts after a 1–2 s magnet settling time for the following masses (total integration time in sec; cumulative duration 12 min; Table 1): ^{184}WO (20), $^{46}\text{Ti}^{48}\text{TiO}_4$ (10), ^{204}Pb (30), ^{206}Pb (30), ^{207}Pb (60), $^{48}\text{Ti}_3\text{O}_4$ (10), ^{208}Pb (30), ^{238}U (50), ^{238}UO (20), $^{232}\text{ThO}_2$ (20), $^{238}\text{UO}_2$ (20).

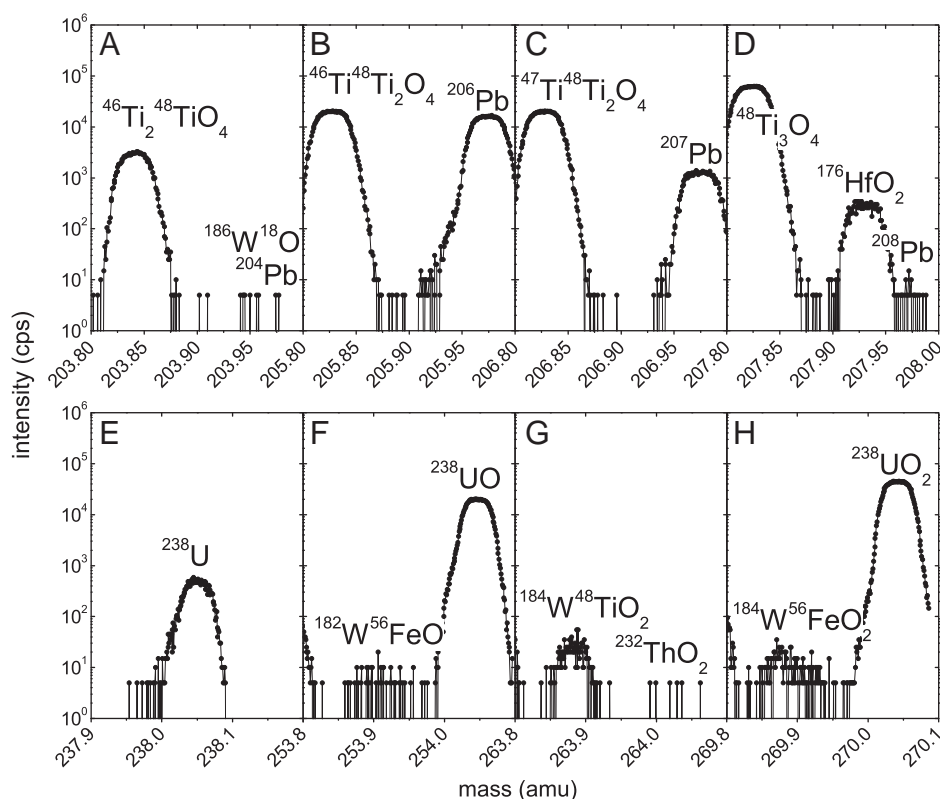


Fig. 2. R10b rutile mass spectra. Secondary ion intensities were acquired using a $\sim 260 \text{ nA } O_2^+$ beam, and recorded at a mass resolving power (MRP) of ~ 4500 .

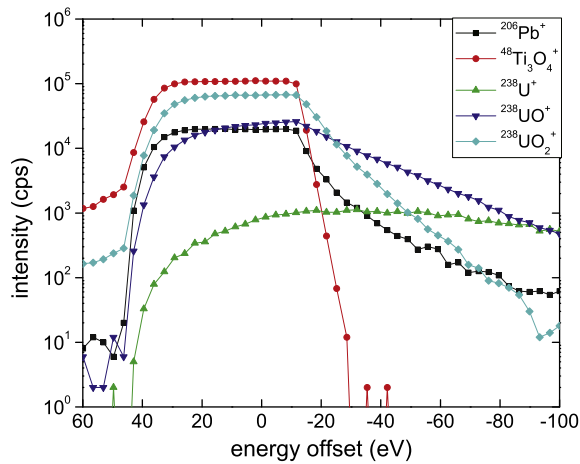


Fig. 3. Energy spectra for R10b rutile secondary ions generated under O_2^+ bombardment. Energy offset is relative to the secondary ion extraction potential of +4.5 kV. Energy band-width 50 eV; all other conditions as in Fig. 2.

^{184}W O was included to estimate W abundances, often the most abundant trace component in rutile. Drift-corrected ratios and intensities were calculated using in-house software ZIPS (version 3.4.1).

3.4. Common Pb correction

Fractionation of Pb-isotopes in SIMS (Stern et al., 2009) is unsystematic, and occurs at a level that is insignificant when compared to other sources of uncertainty. In order to calculate $^{207}Pb/^{206}Pb$ ages, it is thus reasonably neglected (e.g., Compston et al., 1984), and the measured Pb secondary ion signals are only corrected for the contribution of non-radiogenic (common) Pb, conventionally through measurement of the (stable) ^{204}Pb intensity. For rutile, however, the ^{204}Pb peak is interfered by $^{186}W^{18}O$. Resolving this interference would require a high MRP = 10,000 which would lead to a significant reduction in transmission (to ~30% of that at MRP = 4500). Peak-stripping using another WO-species is impractical because of (1) the unpredictability of $^{186}W^{18}O/^{186}W^{16}O$ within the ^{16}O -implanted surface layer from which secondary ions escape, and (2) the very low intensities of $^{183}W^{18}O$ (~50% of the peak at mass/charge = 204). We therefore applied a ^{208}Pb -correction (Compston et al., 1984) for which rutile is ideally suited because of its extremely high U/Th (Zack et al., 2011). Because ^{208}Pb intensities frequently decrease in the course of the analysis, common Pb was reasonably assumed to be overwhelmingly derived from surface contamination, and consequently an anthropogenic Pb composition for Southern California (Sanudo-Wilhelmy and Flegel, 1994) was applied. The percentage of radiogenic $^{208}Pb^*$ was iteratively calculated using measured $^{208}Pb/ThO_2^+$ and age, using the same relative sensitivity factor as for $^{206}Pb/^{238}U$ (see 3.5.). Radiogenic $^{208}Pb^*$ was typically found to be $\ll 10\%$ for the studied rutiles.

3.5. Pb/U relative sensitivity calibration and O_2 flooding

In contrast to Pb-isotopes, SIMS instrumental fractionation for Pb/U isotope species is significant, and requires a correction based on a calibration of standards with known Pb/U. Introduced by Hinthorne et al. (1979), such calibrations involve a relation between the Pb/U isotopic relative sensitivity factors (RSF) determined on a standard to concurrently measured ratios of U-oxides and atomic U. In geochronological SIMS, the Pb/U RSF is defined as (Fig. 4):

$$RSF = \left(^{206}Pb^+ / ^{238}U^+ \right) / \left(^{206}Pb^+ / ^{238}U \right) \quad (1)$$

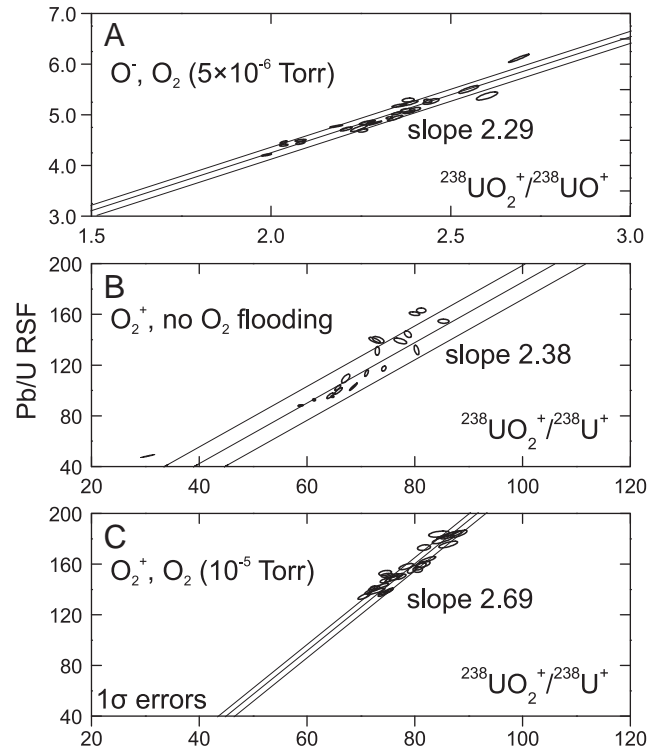


Fig. 4. R10b rutile Pb/U calibration curves. The Pb/U relative sensitivity factor (RSF = measured ratio/true ratio for $^{206}Pb/^{238}U$) is plotted against U-species ratios (see text). Linear regression line and error band is shown.

where $^{206}Pb^*/^{238}U$ is commonly calculated from the age t and decay constant λ of a concordant standard:

$$^{206}Pb^* / ^{238}U = \exp(\lambda_{238} \times t) - 1 \quad (2)$$

(note that in the following, Pb and U refer to ^{206}Pb and ^{238}U , respectively, unless otherwise indicated). For U–Pb analysis of zircon and other accessory minerals the RSF for an unknown is selected from a calibration involving ratios of UO^+/U^+ (Compston et al., 1984), UO_2^+/U^+ (Whitehouse et al., 1997), or UO_2^+/UO^+ (Ireland et al., 1990). Instead of $^{206}Pb^+/U^+$, calibrations involving $^{206}Pb^+/UO^+$ and $^{206}Pb^+/UO_2^+$ have also been developed (e.g., Schuhmacher et al., 1994; Stern and Amelin, 2003). Calibrations are empirically established by linear, quadratic, or power law fitting of standard data (e.g., Hinthorne et al., 1979; Compston et al., 1984; Williams and Claesson, 1987; Ireland et al., 1990). For rutile, Pb/U RSF values are much higher than those for zircon, so that some workers have preferred calibrations of Pb^+/UO^+ vs. UO_2^+/UO^+ (Taylor et al., 2012), although calibrations with Pb^+/U^+ vs. UO_2^+/UO^+ or Pb^+/U^+ vs. UO_2^+/U^+ have also been applied (Li et al., 2011; Zack et al., 2011, respectively).

Secondary ion energy scans (Fig. 3) reveal similar energy distributions for Pb^+ and UO_2^+ , whereas the peak for U^+ (and to lesser extent UO^+) is offset to higher energies (by ~35 eV for U^+). The depletion in low-energy U^+ could reflect near-surface combination reactions between U and O ion species (Williams and Hervig, 2000). Pb and U oxide species, by contrast, have maxima close to the nominal accelerating voltage. Based on the similarity in their energy distribution, we thus prefer a calibration utilizing UO_2^+ and Pb^+ . For O^- beam-generated data, we have determined that the comparatively low U^+ intensities compromise the precision of UO_2^+/U^+ , and therefore followed the procedure in Taylor et al. (2012) of using UO^+ in the denominator. For O_2^+ analysis, the intense primary beam resulting in an elevated secondary ion signal permits precise measurements of Pb^+/U^+ and UO_2^+/U^+ , and consequently, these were used in the calibration. All calibration data were fitted linearly (Fig. 4).

Directing an oxygen jet (O_2 -flooding) onto the sputter region through an orifice in the extraction plate opposite the sample surface significantly enhances Pb^+ yields during primary ion sputtering of zircon using O^- and O_2^- beams (~ 2 -fold; Schuhmacher et al., 1994), although this effect is stronger on the CAMECA ims1270 than on SHRIMP instruments (Ireland and Williams, 2003). Even higher Pb^+ enhancements (~ 10 -fold) were found for baddeleyite under O_2 -flooding on the ims1270/ims1280 (Li et al., 2010; Schmitt et al., 2010). For O^- analysis of rutile, we maximized Pb^+ intensities by adjusting the O_2 -pressure in the sample chamber to $\sim 5 \times 10^{-6}$ Torr (measured by a recessed ion gauge attached to the sample chamber). By contrast, we observed only a minor Pb^+ intensity increase with higher O_2 -pressure during O_2^+ bombardment of rutile which may reflect high abundances of oxygen in the emission volume resulting from implantation of molecular oxygen (see also Zack et al., 2011, for a similar lull in Pb^+ enhancement from O_2 -flooding during O_2^- bombardment).

Besides enhancing Pb^+ yields, an important additional advantage of O_2 -flooding is the mitigation of crystal orientation dependent Pb/U fractionation (Wingate and Compston, 2000) as was demonstrated for baddeleyite by Li et al. (2010) and Schmitt et al. (2010). For rutile, Taylor et al. (2012) documented variable secondary ion intensities in relation to crystal orientation, especially for UO^+ , resulting in a wide range of values along the calibration slope. Taylor et al. (2012) did not use O_2 -flooding. Here, we acquired two sets of rutile analyses using an O_2^+ primary beam: one without, and one with oxygen flooding (1×10^{-5} Torr). Through this, we test the potential of O_2 -flooding to produce a more robust Pb/U calibration (see Section 4.1).

3.6. U/Ti relative sensitivity calibration

Concentrations of U in rutile were calculated by ratioing $^{238}U^+$ to $^{48}Ti_3O_4^+$ intensities, and calculating a RSF by dividing this ratio with the “true” U/Ti ratio for rutile (assuming stoichiometric TiO_2 and 50 ppm U in R10b; Zack et al., 2011). For data acquired with O^- (moderate O_2 flooding at 5×10^{-6} Torr) and O_2^+ without O_2 flooding, a negative correlation exists between the U/Ti RSF and UO^+/U^+ (Fig. 5). We thus used a linear regression through the data to calculate the RSF for each analysis as a function of UO^+/U^+ . Notably, the spread in U–Ti RSF is narrowest for O_2^+ with O_2 flooding, and a correlation between U–Ti RSF and UO^+/U^+ is absent (Fig. 5). Because U concentrations in R10b are only known to within $\pm 20\%$ (Luvizotto et al., 2009), we estimate this to be the uncertainty for the U concentrations reported here (see Section 4.2.).

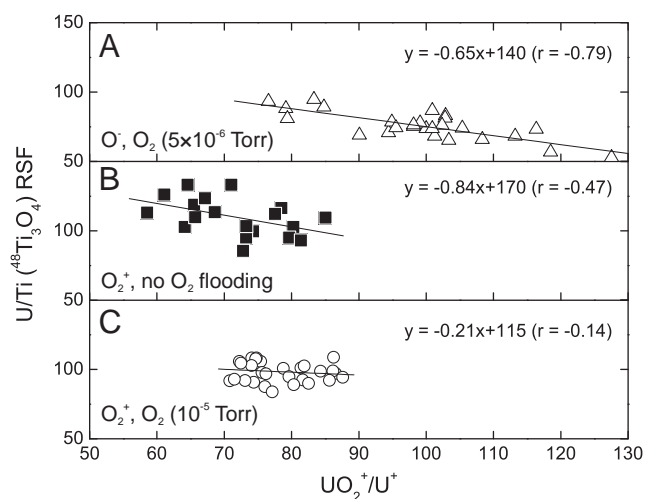


Fig. 5. R10b rutile U/Ti calibration curves. U/Ti RSF ($^{48}Ti_3O_4$) is the measured $U^+/^{48}Ti_3O_4^+$ divided by the U/Ti mass ratio = 8.34×10^{-5} for 50 ppm U in stoichiometric TiO_2 . Linear regression is used to estimate RSF factors for calculation of U concentrations.

3.7. Sputter depth and volume measurements

After SIMS analysis, the Au coating was removed from the mount through a gentle polish with 1 μm diamond suspension. The topography of the analysis craters was then determined using a MicroXAM optical interferometer. The steepness and depth of the O_2^+ pits resulted in poor reflectivity, especially from the crater bottom (Fig. 1), and we estimate O_2^+ pit dimensions to within approximately $\pm 1 \mu m$, and those of O^- to $\pm 0.1 \mu m$.

4. Results

4.1. SIMS sputtering behavior and sensitivity

All rutiles analyzed in this study were conductive during bombardment with O^- or O_2^+ . Minor charging ($< \pm 10$ V) occurred in a few crystals. No detrimental effects on secondary ion intensities or elemental ratios were observed in these cases. Sputter yields (Y = sputtered atom flux normalized to the primary atom flux; Table 2) average 0.74 for the O^- beam (with O_2 -flooding) overlapping with average $Y = 0.55$ for O_2^+ bombardment under ultra-high vacuum (no O_2 -flooding), excluding four enigmatically high outliers for O^- (Fig. 6). Rutile thus behaves somewhat differently from silicon where O_2^+ beams produce higher Y compared to O^- , which is attributed to the higher efficiency for target atom ejection by low-angle (grazing) primary ion trajectories (Franzreb et al., 2004). The decrease in Y for O_2^+ with increasing O_2 -pressure (average $Y = 0.24$ at 1×10^{-5} Torr O_2 -flooding), however, is consistent with trends for silicon in Franzreb et al. (2004).

For precise U–Pb geochronology of accessory minerals, the limiting factors lie principally in the sensitivity for Pb, and the abundance of radiogenic Pb (i.e., the ability to perform a common Pb correction). For Pb^+ , useful yields (UY) are highest for O^- with O_2 -flooding (UY = 3.6%) and about 50% of this value for the O_2^+ beam without correcting for the smaller field aperture relative to the size of the crater in O_2^+ analysis (UY = 1.6% and 1.7% with and without O_2 -flooding, respectively). UY for U^+ is extremely low for rutile under all experimental conditions explored here (UY = 0.02%; Table 2). By contrast, UYs for molecular UO_2^+ are characteristically elevated for rutile, and are $\sim 50\%$ of those for $^{206}Pb^+$ (Table 2). When accounting for the $\sim 60\%$ reduced transmission from the smaller field aperture in O_2^+ analysis, UY values are within 75% of those for O^- (Table 1).

Because Th abundances in rutile are very low, ^{208}Pb intensities should almost exclusively represent common lead. Most often, this signal decreases throughout an analysis, suggesting that a major contributor to the ^{208}Pb signal is contamination on the rutile surface. When the sample is sputtered for a suitable interval prior to data collection, this ‘pre-sputtering’ removes surface contamination to the point where the percentage of radiogenic lead (with or without flooding) is $> 99.8\%$ ($^{206}Pb^*$) and 97% ($^{207}Pb^*$), whereas those for O^- after identical pre-sputter durations are $> 98.4\%$ ($^{206}Pb^*$) and 80% ($^{207}Pb^*$). This is due to the faster sputtering of the more intense O_2^+ beam coupled with its shallower penetration depth. This efficiently exposes uncontaminated interior domains with less mixing of surface contaminants (e.g., Williams et al., 2006).

We also determined that the stability of the Pb/U calibration is significantly improved using O_2 -flooding: without O_2 -flooding, UO_2^+/U^+ (average = 70) varied by $\pm 20\%$, whereas with O_2 -flooding the range was only $\pm 13\%$ (average = 78; Fig. 4). There is also a strong correlation between sputter yield and UO_2^+/U^+ for O_2^+ without O_2 -flooding (Fig. 6). Data obtained at high oxygen pressures (O_2^+ at 1×10^{-5} Torr O_2) lack this correlation, and show an overall more restricted range in UO_2^+/U^+ compared to O_2^+ without O_2 flooding (Fig. 6). Without O_2 -flooding, the Pb^+/U^+ vs. UO_2^+/U^+ calibration resulted in a poor linear fit with $\sim 30\%$ scatter in the apparent Pb/U RSF (Fig. 4). Although this could potentially be improved by a quadratic, or power law fit, we found that the excessively large spread of the calibration data is a significant source of

Table 2
Summary of U–Pb ages for rutile standards.

		$^{207}\text{Pb}^*/^{206}\text{Pb}^*$ age Ma				$^{206}\text{Pb}^*/^{238}\text{U}$ age Ma					Pb^*/U concordia age Ma				
		err	MSWD	Δ %	1 s.d. %	err	MSWD	Δ %	1 s.d. %	err	MSWD	Δ %	n		
<i>R10b (ID-TIMS: 1090 ± 5 Ma; Luvizotto et al., 2009)</i>															
Session 1	O [−]	1090 ± 6	0.86	0.00	1.4	1090^{a}	± 7	0.64	−	1.9	1088 ± 3	0.45	−0.18	26	
Session 2	O ₂ ⁺ (no O ₂ flooding)	1090 ± 5	3.20	0.00	0.10	−	−	−	−	−	−	−	−	20	
Session 3	O ₂ ⁺ (O ₂ flooding)	1084 ± 6	1.30	−0.18	0.14	1090^{a}	± 15	0.67	−	3.2	1084 ± 3	0.58	−0.55	30	
<i>R19 (ID-TIMS: 489.5 ± 0.9 Ma; Zack et al., 2011)</i>															
Session 1	O [−]	501 ± 26	0.67	2.35	11	490	± 5	0.83	0.10	2.2	490 ± 3	0.25	0.10	20	
Session 2	O ₂ ⁺ (no O ₂ flooding)	502 ± 12	1.50	2.55	5.8	−	−	−	−	−	−	−	−	14	
Session 3	O ₂ ⁺ (O ₂ flooding)	$521^{\text{b}} \pm 22$	1.00	7.46	7.8	486	± 17	1.8	−0.72	5.2	490^{b}	± 14	−0.72	14	
<i>JIMP-1B (ID-TIMS 2625 Ma; Clark et al., 2000)</i>															
Session 1	O [−]	2642 ± 3	1.80	0.65	0.2	2631	± 22	0.86	0.77	1.7	2641 ± 7	1.7	0.61	20	
Session 2	O ₂ ⁺ (no O ₂ flooding)	2645	± 2	3.80	0.76	1.0	−	−	−	−	−	−	−	−	
Session 3	O ₂ ⁺ (O ₂ flooding)	2642 ± 2	1.30	0.65	0.2	2638	± 50	0.37	0.50	2.1	2642 ± 3	0.23	0.64	12	

err = 2 sigma errors of weighted average times square-root of MSWD if > 1.

Average primary beam currents: 19 nA (session 1); 330 nA (session 2); 130 nA (session 3).

Δ % = relative deviation from ID TIMS value.

1 s.d. % = one standard deviation (relative).

^a Normalized to ID TIMS value for relative sensitivity factor calibration.

^b Excluding one analysis.

* ²⁰⁸Pb-corrected radiogenic.

uncertainty for U–Pb ages, and consequently we only calculated U–Pb ages for data generated using O₂-flooding.

4.2. SIMS Pb–Pb and U–Pb age precision and accuracy

Estimated U concentrations (relative to R10b) average ~20 ppm for R19 and ~100 ppm for JIMP-1B (Table 2). R13 and SQR36 have average U abundances of ~20 ppm and ~300 ppm, respectively, although U in SQR36 is highly variable (between ~1 and 500 ppm; Electronic Appendix). Tungsten as one of the most abundant trace element in rutile (e.g., Luvizotto et al., 2009) is generally present at abundances <1000 ppm (Electronic Appendix). For R10b and JIMP-1B, the average $^{207}\text{Pb}^*/^{206}\text{Pb}^*$ ages (after ²⁰⁸Pb-correction) are within 1% of the known values (Table 2). The highest-precision $^{207}\text{Pb}^*/^{206}\text{Pb}^*$ ages are obtained for O₂⁺ (with and without O₂-flooding) which reflects that these analyses – at high sputter rates afforded by the intense O₂⁺ beam – yielded the most radiogenic Pb compositions. For

Early Palaeozoic rutile R19, however, $^{207}\text{Pb}^*/^{206}\text{Pb}^*$ ages are comparatively imprecise, and precision and accuracy of the U–Pb ages becomes increasingly relevant relative to the Pb–Pb ages. For sputtering with O₂-flooding (for both, O[−] and O₂⁺), UO₂⁺/UO⁺ and UO₂⁺/U⁺ are similar for R10b and the “unknown” rutiles analyzed under the same conditions. This is a first-order calibration requirement because a mismatch between standards and unknowns introduces potential age bias due to extrapolation of the calibration beyond the range defined by the standards. Without O₂-flooding, a wider range in calibration values and less overlap between R10b and “unknowns” is observed. Because of this, we have refrained from calculating $^{206}\text{Pb}^*/^{238}\text{U}$ and concordia ages for data acquired without O₂-flooding, and only U–Pb rutile ages acquired with O₂-flooding are deemed reliable (see also 4.1).

The reproducibility of individual $^{206}\text{Pb}^*/^{238}\text{U}$ age spot analyses is ~2% for O[−] (1 standard deviation s.d.; Table 2). For R10b and JIMP-1B under O₂⁺ bombardment, spot-to-spot reproducibility is between ~2 and 3%, with a somewhat higher variability for R19 (~5%; Table 2). For R19, the high MSWD of ~10 for the O₂⁺ analysis reflects the smaller counting error, and potentially some minor age heterogeneity. Importantly, the precision of $^{206}\text{Pb}^*/^{238}\text{U}$ and concordia ages for averages of 15 to 30 spot analyses is <1% for all rutiles analyzed here, independent of the primary ion species used (Table 2; Fig. 7). For R10 and R19, SIMS and TIMS ages overlap within analytical uncertainty. The TIMS age for JIMP-1B falls outside the analytical uncertainty for SIMS $^{207}\text{Pb}^*/^{206}\text{Pb}^*$ and concordia ages (Table 2); however, TIMS uncertainties are not reported in Clark et al. (2000). Overall average $^{206}\text{Pb}^*/^{238}\text{U}$ age accuracy is <1%.

R13 and SQR36 (Electronic Appendix) lack ID TIMS data, and therefore the SIMS ages cannot be independently assessed for accuracy. However, we find that their $^{207}\text{Pb}^*/^{206}\text{Pb}^*$ and $^{206}\text{Pb}^*/^{238}\text{U}$ ages (against Pb/U calibration standard R10b) are equivalent in precision to those of R19 and JIMP-1B, with O[−] and O₂⁺-generated ages in excellent agreement. R13 yields a concordia age (O[−]: 504 ± 4 Ma; MSWD = 0.2; n = 8; O₂⁺: 505 ± 6 Ma; MSWD = 2.2; n = 10; all with O₂ flooding) which overlaps with the end of peak metamorphism of the Central Zone of the Damara Belt (~510 Ma; Gray et al., 2006). The SQR36 concordia age (O[−]: 1998 ± 6 Ma; MSWD = 2.1; n = 15; O₂⁺: 2001 ± 7 Ma; MSWD = 1.9; n = 13; all with O₂ flooding) is in accordance with the age of the last high-grade metamorphic overprint of Musina basement rocks (~2025 Ma; Zeh et al., 2010).

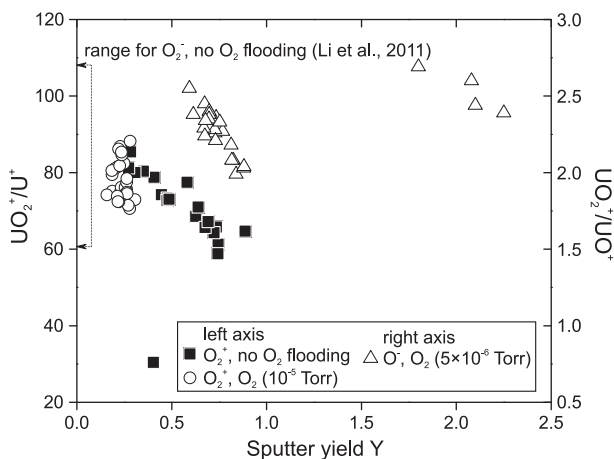


Fig. 6. UO₂⁺/U⁺ (UO₂⁺/UO⁺) fractionation vs. depth sputter rate for different primary beam, and O₂ flooding conditions. Comparison with published data (Li et al., 2011) indicates a comparatively high variability of UO₂⁺/U⁺ for an O[−] beam without O₂ flooding.

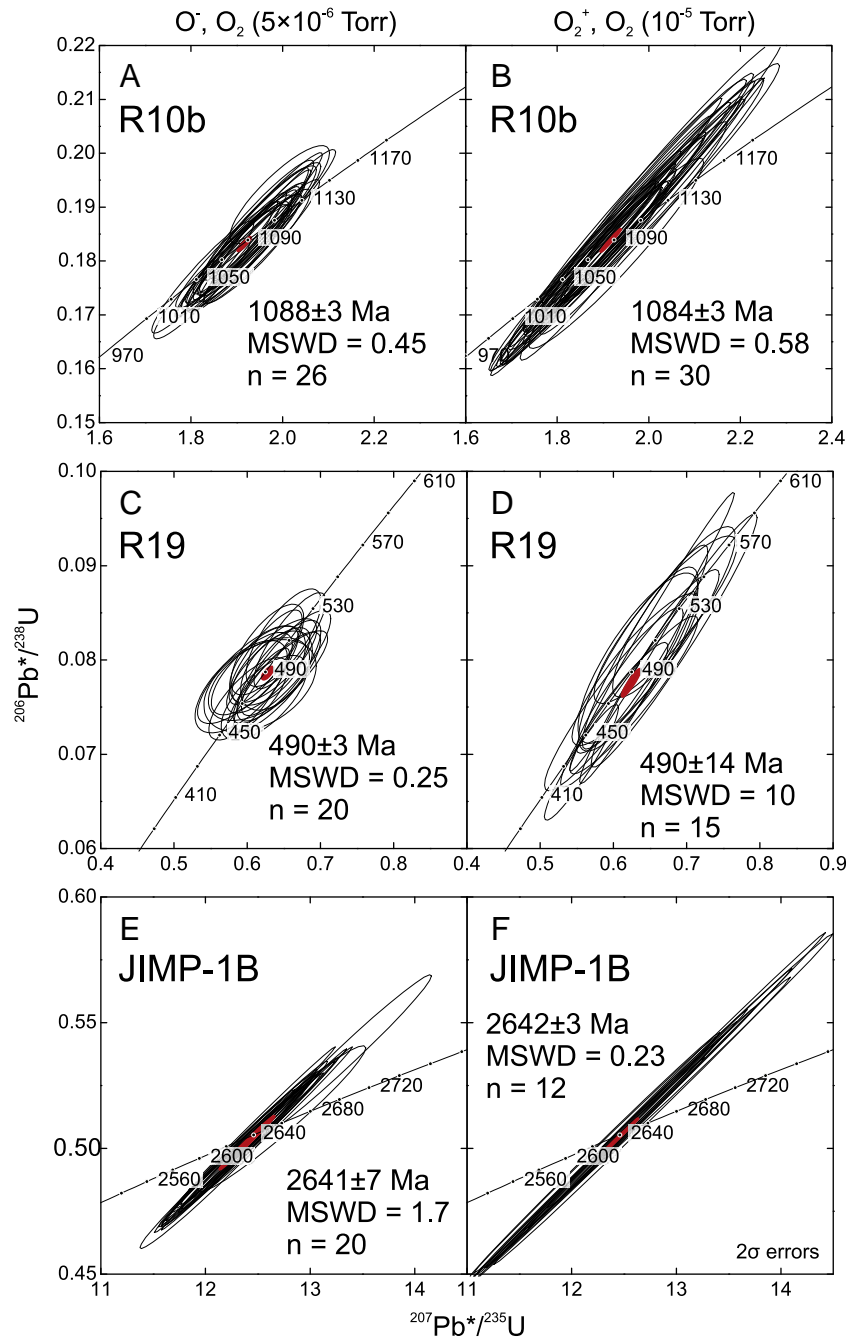


Fig. 7. Concordia U–Pb ages for three rutile standards analyzed by SIMS. Left panels are for data acquired with a conventional O^- beam (O_2 flooding at 5×10^{-6} Torr); right panels show data for O_2^+ bombardment with O_2 flooding (1×10^{-5} Torr). Individual spot analyses are black ellipses; weighted averages are red ellipses. (For interpretation of the references to color in this figure legend, the reader is referred to the web version of this article.)

5. Discussion

5.1. Mitigation of crystal orientation effects in SIMS U–Pb rutile dating

We have documented that randomly oriented rutile fragments have significantly different sputter yields (Y), which vary by more than 300% for rutile O_2^+ bombardment without O_2 -flooding (Fig. 6). Y also negatively correlates with UO_2^+/U^+ and UO_2^+/UO^+ , except for analysis conditions of O_2^+ with O_2 -flooding (Fig. 6). We have not directly determined crystal orientation relative to the incoming beam, but given the chemical homogeneity of the rutile crystals studied here, crystal orientation effects are the only plausible explanation for the strong sputter yield heterogeneities. We suggest that crystal

orientation dependent variations in Y are primarily responsible for the unusually wide range of UO_2^+/UO^+ and UO_2^+/U^+ calibration data for rutile noticed by us and previous workers (Li et al., 2011; Taylor et al., 2012). Taylor et al. (2012) proposed ion tunneling vs. target atom collisions along certain crystallographic directions for this behavior. Because sputtering at high O_2 -pressure (O_2^+ with O_2 -flooding) produced the least variation in Y (Fig. 6), we conclude that O_2 -flooding strongly reduces the extent to which crystal-orientation dependent sputter rate variations affect UO_2^+/U^+ .

Fig. 6 aids in explaining the empirical evidence for the mitigating effects of a surficial layer of oxygen atoms for scatter of Pb/U RSF calibrations found here and elsewhere (Li et al., 2010; Schmitt et al., 2010). First, the values and variability for Y are smaller for O_2^+ with

O₂-flooding compared to no O₂-flooding. Second, the UO₂⁺/U⁺ overlaps for spots with small Y without O₂-flooding and the generally smaller Y with O₂-flooding. The negative correlation between Y and the ratio of more oxidized over less oxidized U species (e.g., UO₂⁺/U⁺) suggests that the surface layer from which ions escape becomes progressively more depleted in oxygen at high sputter rates. This depletion can be compensated by O₂-flooding ("backfill" of oxygen into the surface layer), resulting in a more restricted range of values for UO₂⁺/U⁺. Because of the correlation between UO₂⁺/U⁺ and Pb/U RSF (Fig. 4), less variability in UO₂⁺/U⁺ improves the reproducibility of Pb/U RSF.

Moreover, variability in Pb/U RSF, even when tightly correlated with a U species ratio, can introduce U–Pb age bias if calibration values for standards and unknown are mismatched (Taylor et al., 2012). With elevated O₂ pressure, we find more confined Pb/U and U/Ti calibrations (Figs. 4 and 5), thus limiting the potential of standard-sample mismatch.

Because the crystal chemistry of natural rutile studied here is largely stoichiometric (TiO₂ with minor components collectively present at levels <1 wt.%; e.g., Zack et al., 2011), we caution that compositional variability in rutile ("matrix effects") cannot be completely ruled out as a cause for U–Pb age bias in case of rutile enriched in trace and minor components (e.g., Fe, Nb, Sn, Sb, Ta, W; Zack et al., 2002). During subsequent analyses of a different set of R10b grains using O₂⁺ with O₂-flooding (unpublished data), we have encountered two R10b anomalous spots that deviate from the calibration curve, yielding ~30% older ²⁰⁶Pb*/²³⁸U ages. These deviant R10b analyses are also characterized by highly elevated (100×) ThO₂⁺ intensities. The cause for this heterogeneity remains obscure, but fortunately, such anomalous spots are readily recognized by their unusually low U/Th.

5.2. Potential of SIMS O₂⁺ rutile geochronology

SIMS sensitivity for Pb⁺ in rutile (based on comparison of useful yields) is more than two-orders of magnitude higher than for quadrupole LA-ICP-MS (~3–4% vs. ~0.01%, respectively; (Zack et al., 2011). For comparison, sector field LA-ICP-MS sensitivities are intermediate (U and Pb UY = ~0.3% for zircon; Frei and Gerdes, 2009). Excavation rates, however, are orders-of-magnitude smaller in SIMS relative to LA-ICP-MS: for the beam conditions used here, O[−] depth sputter rates (at ~20 nA) are 100-times less, and those for O₂⁺ (at ~200 nA) are approximately 10-times less than ablation rates in Zack et al. (2011). Consequently, SIMS secondary ion intensities are typically lower than for LA-ICP-MS, requiring longer counting times to achieve the same precision. In consequence, Pb–Pb and U–Pb analysis for rutile by SIMS is best suited for conditions where the amount of analyte is limited, i.e., in the case of young and/or very small samples such as complex rutile crystals, micro-rutile, or rutile inclusions.

The observation that for O₂⁺ bombardment, Pb⁺ UY is lower than that for O[−] (Table 1) can be qualitatively explained by two factors: (1) a lower secondary ion extraction voltage relative to O[−] which is required to maintain high primary ion impact energies, and (2) narrowing the field aperture to block ions from peripheral sputtering of the Gaussian O₂⁺ beam. For CAMECA 3f and 6f instruments, estimates for the decrease in UY at 4.5 kV relative to 10 kV are 50–70%, all other conditions remaining equal (Hervig et al., 2006). The somewhat stronger decrease observed here is likely due to the additional transmission reduction which results from narrower field aperture settings selected to suppress admission of secondary ions derived from the broad tail of the Gaussian O₂⁺ beam (Table 1). This moderate penalty in Pb sensitivity for O₂⁺ analysis at +4.5 kV secondary potential is largely offset by the higher secondary ion intensities resulting from the more intense (~10×) O₂⁺ beam.

The high-brightness O₂⁺ source has traditionally been underutilized in geological SIMS, mainly because of the difficulties in maintaining stable charge compensation for insulators. There is, however, strong

potential to further develop O₂⁺ sputtering of geological (semi-)conductor materials, or even insulators if charge compensation can be achieved (e.g., Genareau et al., 2007). Future improvements in rutile geochronology using O₂⁺ involve simultaneous detection of ²⁰⁶Pb, ²⁰⁷Pb, and ²⁰⁸Pb (with additional detection of ²⁰⁴Pb being possible on the ims1270, but of questionable use because of the ¹⁸⁶W¹⁸O interference; Fig. 2). This can increase precision for ²⁰⁷Pb/²⁰⁶Pb ages, enable analysis of low-radiogenic Pb rutile (e.g., Topuz et al., 2012), and shorten analysis durations (e.g., for detrital rutile studies). Moreover, analyzing abundant, but well resolved, cluster ions in the mass range between 196 and 270 such as ¹⁸⁴WO, ¹⁷⁶HfO₂ (Fig. 2D), or ⁹⁰Zr₂O (not shown) in tandem with U–Pb geochronology can provide additional information for rutile provenance or thermometry (Zr-in-rutile; Tomkins et al., 2007; Watson et al., 2006; Zack et al., 2004a, b). There are also other conductive minerals for which O₂⁺ analysis can be advantageous. For reconnaissance, we have determined that the O₂⁺ beam without charge compensation can be applied to Fe–Ti oxides (magnetite, hematite, ilmenite), cassiterite, uraninite, and columbite-tantalite.

6. Conclusions

- (1) Rutile is conductive under ion beam bombardment; this permits analysis with an intense (~100–200 nA) O₂⁺ primary ion beam at a lateral resolution equivalent to SIMS using negative O primary ion beams (~20–35 μm beam diameter);
- (2) Rapid surface sputtering using an intense O₂⁺ beam efficiently removes surficial Pb, resulting in highly radiogenic and precise ²⁰⁷Pb*/²⁰⁶Pb* ages (after a ²⁰⁸Pb-based common Pb correction);
- (3) Sensitivity of SIMS is high for rutile with useful yields UY between 3–4% and 1–2% for Pb⁺ and UO₂⁺, respectively, whereas those for U⁺ are strongly suppressed (UY = 0.02%);
- (4) O₂ flooding reduces crystal orientation dependent variability in depth sputter rate, and the resulting elemental and molecular fractionations. This favors coherency in Pb/U relative sensitivity calibrations;
- (5) Under conditions of O₂ flooding, SIMS ²⁰⁷Pb*/²⁰⁶Pb* and ²⁰⁶Pb*/²³⁸U rutile age averages agree within <1% with ID TIMS ages;
- (6) The combination of using an O₂⁺ primary beam and O₂ flooding is advantageous for precise and accurate analysis of rutile at high spatial resolution and yield.

Acknowledgments

Delia Rösel is thanked for mineral separation of JIMP-1B; Armin Zeh for providing SQR36. We are grateful for technical assistance by Lvcian Vltava and George Jarzebinski. Constructive and insightful reviews by Richard Hervig and Richard Stern are acknowledged. TZ thanks the German Science Foundation (DFG) for support (Za285/6-2 and Za285/7-1). The ion microprobe facility at UCLA is partly supported by a grant from the Instrumentation and Facilities Program, Division of Earth Sciences, National Science Foundation.

Appendix A. Supplementary data

Supplementary data to this article can be found online at <http://dx.doi.org/10.1016/j.chemgeo.2012.09.023>.

References

- Bromiley, G.D., Hilairt, N., 2005. Hydrogen and minor element incorporation in synthetic rutile. *Mineralogical Magazine* 69 (3), 345–358.
- Clark, D.J., Hensen, B.J., Kinny, P.D., 2000. Geochronological constraints for a two-stage history of the Albany-Fraser Orogen, Western Australia. *Precambrian Research* 102 (3–4), 155–183.
- Coath, C.D., Long, J.V.P., 1995. A high-brightness duoplasmatron ion-source for microprobe secondary-ion mass-spectrometry. *The Review of Scientific Instruments* 66 (2), 1018–1023.

- Colasanti, C.V., Johnson, E.A., Manning, C.E., 2011. An experimental study of OH solubility in rutile at 500–900 degrees C, 0.5–2 GPa, and a range of oxygen fugacities. *American Mineralogist* 96 (8–9), 1291–1299.
- Compston, W., Williams, I.S., Meyer, C.E., 1984. U–Pb geochronology of zircons from lunar breccia 73217 using a sensitive high mass-resolution ion microprobe. *Journal of Geophysical Research* 89 (Suppl.(B)), 525–534.
- Davis, W.J., 1997. U–Pb zircon and rutile ages from granulite xenoliths in the Slave province: evidence for mafic magmatism in the lower crust coincident with Proterozoic dike swarms. *Geology* 25 (4), 343–346.
- Foley, S.F., Barth, M.G., Jenner, G.A., 2000. Rutile/melt partition coefficients for trace elements and an assessment of the influence of rutile on the trace element characteristics of subduction zone magmas. *Geochimica et Cosmochimica Acta* 64 (5), 933–938.
- Franzreb, K., Lorincik, J., Williams, P., 2004. Quantitative study of oxygen enhancement of sputtered ion yields. I. Argon ion bombardment of a silicon surface with O-2 flood. *Surface Science* 573 (2), 291–309.
- Frei, D., Gerdes, A., 2009. Precise and accurate in situ U–Pb dating of zircon with high sample throughput by automated LA-SF-ICP-MS. *Chemical Geology* 261 (3–4), 261–270.
- Genareau, K., Hervig, R., Clarke, A., 2007. Geochemical variations in late-stage growth of volcanic phenocrysts revealed by SIMS depth-profiling. *American Mineralogist* 92 (8–9), 1374–1382.
- Gray, D.R., Foster, D.A., Goscombe, B., Passchier, C.W., Trouw, R.A.J., 2006. Ar-⁴⁰/Ar-³⁹ thermochronology of the Pan-African Damara Orogen, Namibia, with implications for tectonothermal and geodynamic evolution. *Precambrian Research* 150 (1–2), 49–72.
- Harrison, T.M., Trail, D., Schmitt, A.K., Watson, E.B., 2007. Rutile ²⁰⁷Pb–²⁰⁶Pb ages in the Jack Hills quartzite, Western Australia. *Geochimica et Cosmochimica Acta* 71 (15), A383.
- Hervig, R.L., Mazdab, F.K., Williams, P., Guan, Y.B., Huss, G.R., Leshin, L.A., 2006. Useful ion yields for Cameca IMS 3f and 6f SIMS: limits on quantitative analysis. *Chemical Geology* 227 (1–2), 83–99.
- Hinthorne, J.R., Andersen, C.A., Conrad, R.L., Lovering, J.F., 1979. Single-grain Pb-²⁰⁷Pb–²⁰⁶Pb age-determinations with a 10-Mu-M spatial-resolution using the ion microprobe mass analyzer (IMMA). *Chemical Geology* 25 (4), 271–303.
- Hunter, J.L., 2009. Improving depth profile measurements of natural materials: lessons learned from electronic materials depth-profiling. In: Fayek, M. (Ed.), *Secondary Ion Mass Spectrometry in the Earth Sciences: Gleaning the Big Picture from a Small Spot*. Short Course Series. Mineralogical Association of Canada (MAC), Québec, pp. 133–148.
- Ireland, T.R., Williams, I.S., 2003. Considerations in zircon geochronology by SIMS. *Zircon. Reviews in Mineralogy and Geochemistry* 215–241.
- Ireland, T.R., Compston, W., Williams, I.S., Wendt, I., 1990. U–Th–Pb systematics of individual perovskite grains from the Allende and Murchison carbonaceous chondrites. *Earth and Planetary Science Letters* 101 (2–4), 379–387.
- Kitagawa, H., Kunisada, T., Yamada, Y., Kubo, S., 2010. Effect of boron-doping on thermoelectric properties of rutile-type titanium dioxide sintered materials. *Journal of Alloys and Compounds* 508 (2), 582–586.
- Klemme, S., Prowatke, S., Hametner, K., Gunther, D., 2005. Partitioning of trace elements between rutile and silicate melts: implications for subduction zones. *Geochimica et Cosmochimica Acta* 69 (9), 2361–2371.
- Kooijman, E., Mezger, K., Berndt, J., 2010. Constraints on the U–Pb systematics of metamorphic rutile from in situ LA-ICP-MS analysis. *Earth and Planetary Science Letters* 293 (3–4), 321–330.
- Li, Q.L., Li, X.H., Liu, Y., Tang, G.Q., Yang, J.H., Zhu, W.G., 2010. Precise U–Pb and Pb–Pb dating of Phanerozoic baddeleyite by SIMS with oxygen flooding technique. *Journal of Analytical Atomic Spectrometry* 25 (7), 1107–1113.
- Li, Q.L., Lin, W., Su, W., Li, X.H., Shi, Y.H., Liu, Y., Tang, G.Q., 2011. SIMS U–Pb rutile age of low-temperature eclogites from southwestern Chinese Tianshan, NW China. *Lithos* 122 (1–2), 76–86.
- Luvizotto, G.L., Zack, T., Meyer, H.P., Ludwig, T., Triebold, S., Kronz, A., Münker, C., Stockli, D.F., Prowatke, S., Klemme, S., Jacob, D.E., von Eynatten, H., 2009. Rutile crystals as potential trace element and isotope mineral standards for microanalysis. *Chemical Geology* 261 (3–4), 346–369.
- Meinhold, G., 2010. Rutile and its applications in earth sciences. *Earth-Science Reviews* 102 (1–2), 1–28.
- Mezger, K., Hanson, G.N., Bohlen, S.R., 1989. High-precision U–Pb Ages of Metamorphic Rutile — application to the cooling history of high-grade terranes. *Earth and Planetary Science Letters* 96 (1–2), 106–118.
- Nowotny, M.K., Sheppard, L.R., Bak, T., Nowotny, J., 2008. Defect chemistry of titanium dioxide. application of defect engineering in processing of TiO₂-based photocatalysts. *Journal of Physical Chemistry C* 112 (14), 5275–5300.
- Pivovarov, A.L., Stevie, F.A., Griffis, D.P., 2004. Improved charge neutralization method for depth profiling of bulk insulators using O-2(+) primary beam on a magnetic sector SIMS instrument. *Applied Surface Science* 231, 786–790.
- Sanudo-Wilhelmy, S.A., Flegal, A.R., 1994. Temporal variations in lead concentrations and isotopic composition in the Southern California Bight. *Geochimica et Cosmochimica Acta* 58 (15), 3315–3320.
- Schmitt, A.K., Chamberlain, K.R., Swapp, S.M., Harrison, T.M., 2010. In situ U–Pb dating of micro-baddeleyite by secondary ion mass spectrometry. *Chemical Geology* 269 (3–4), 386–395.
- Schuhmacher, M., De Chambost, E., McKeegan, K.D., Harrison, T.M., Migeon, H., 1994. In situ dating of zircon with the CAMECA ims 1270. Secondary ion mass spectrometry. In: Benninghoven, A., Werner, H.W., Shimizu, R., Nihei, Y. (Eds.), *SIMS IX*. John Wiley & Sons, pp. 919–922.
- Stern, R.A., Amelin, Y., 2003. Assessment of errors in SIMS zircon U–Pb geochronology using a natural zircon standard and NIST SRM 610 glass. *Chemical Geology* 197 (1–4), 111–142.
- Stern, R.A., Bodorkos, S., Kamo, S.L., Hickman, A.H., Corfu, F., 2009. Measurement of SIMS instrumental mass fractionation of Pb isotopes during zircon dating. *Geochemical and Geoanalytical Research* 33 (2), 145–168.
- Taylor, R., Clark, C., Reddy, S.M., 2012. The effect of grain orientation on secondary ion mass spectrometry (SIMS) analysis of rutile. *Chemical Geology* 300, 81–87.
- Tomkins, H.S., Powell, R., Ellis, D.J., 2007. The pressure dependence of the zirconium-in-rutile thermometer. *Journal of Metamorphic Geology* 25 (6), 703–713.
- Topuz, G., Göçmengil, G., Rolland, Y., Çelik, Ö.F., Zack, T., Schmitt, A.K., 2012. Jurassic accretionary complex and ophiolite from northeast Turkey: no evidence for the Cimmerian continent. *Geology*. <http://dx.doi.org/10.1130/G33577.1>.
- Vry, J.K., Baker, J.A., 2006. LA-MC-ICPMS Pb–Pb dating of rutile from slowly cooled granulites: confirmation of the high closure temperature for Pb diffusion in rutile. *Geochimica et Cosmochimica Acta* 70 (7), 1807–1820.
- Watson, E.B., Wark, D.A., Thomas, J.B., 2006. Crystallization thermometers for zircon and rutile. *Contributions to Mineralogy and Petrology* 151 (4), 413–433.
- Whitehouse, M.J., Claesson, S., Sunde, T., Vestin, J., 1997. Ion microprobe U–Pb zircon geochronology and correlation of Archaean gneisses from the Lewisian Complex of Grunard Bay, northwestern Scotland. *Geochimica et Cosmochimica Acta* 61 (20), 4429–4438.
- Williams, I.S., Claesson, S., 1987. Isotopic evidence for the Precambrian provenance and Caledonian metamorphism of high-grade paragneisses from the Seve Nappes, Scandinavian Caledonides .2. Ion microprobe zircon U–Th–Pb. *Contributions to Mineralogy and Petrology* 97 (2), 205–217.
- Williams, P., Hervig, R.L., 2000. Associative detachment reactions in oxygen-sputtered uranium. *Secondary Ion Mass Spectrometry*. In: Benninghoven, A., Bertrand, P., Migeon, H.N., Werner, H.W. (Eds.), *SIMS XII*. Elsevier, pp. 139–142.
- Williams, P., Sobers Jr., R.C., Franzreb, K., Lörincik, J., 2006. Quantitative fundamental SIMS studies using ¹⁸O implant standards. *Applied Surface Science* 252 (19), 6429–6432.
- Wingate, M.T.D., Compston, W., 2000. Crystal orientation effects during ion microprobe U–Pb analysis of baddeleyite. *Chemical Geology* 168 (1–2), 75–97.
- Zack, T., Kronz, A., Foley, S.F., Rivers, T., 2002. Trace element abundances in rutiles from eclogites and associated garnet mica schists. *Chemical Geology* 184 (1–2), 97–122.
- Zack, T., Moraes, R., Kronz, A., 2004a. Temperature dependence of Zr in rutile: empirical calibration of a rutile thermometer. *Contributions to Mineralogy and Petrology* 148 (4), 471–488.
- Zack, T., von Eynatten, H., Kronz, A., 2004b. Rutile geochemistry and its potential use in quantitative provenance studies. *Sedimentary Geology* 171 (1–4), 37–58.
- Zack, T., Stockli, D.F., Luvizotto, G.L., Barth, M.G., Belousova, E., Wolfe, M.R., Hinton, R.W., 2011. In situ U–Pb rutile dating by LA-ICP-MS: Pb–208 correction and prospects for geological applications. *Contributions to Mineralogy and Petrology* 162 (3), 515–530.
- Zeh, A., Gerdes, A., Barton, J., Klemd, R., 2010. U–Th–Pb and Lu–Hf systematics of zircon from TTG's, leucosomes, meta-anorthosites and quartzites of the Limpopo Belt (South Africa): Constraints for the formation, recycling and metamorphism of Palaeoarchaean crust. *Precambrian Research* 179 (1–4), 50–68.